PCCP

Accepted Manuscript

ROYAL SOCIETY OF CHEMISTRY

www.rsc.org/pccp

Dendritic α-Fe₂O₃/TiO₂ nanocomposites with improved visible light photocatalytic activity

Xin Li, Huiming Lin*, Xiang Chen, Hao Niu, Jiuyu Liu, Ting Zhang, Fengyu Qu*

College of Chemistry and Chemical Engineering, Harbin Normal University, P. R. China, Harbin 150025

Corresponding author: Tel/Fax: +86 0451 88060653.

E-mail address: qufengyu@hrbnu.edu.cn and linhuiming@hrbnu.edu.cn

Abstract

The design and synthesis of unique novel heterostructures for high-performance photocatalytic activity has exerted a tremendous fascination and has recently attracted intensive attention. In this paper, a branch-like α-Fe$_2$O$_3$/TiO$_2$ heterostructure is synthesized controllably through an electrospinning method combined with a hydrothermal approach. The backbone of the heterostructure is composed of 3D porous TiO$_2$ nanofibers (~70 nm in diameter) network with plenty of α-Fe$_2$O$_3$ nanorods (100~200 nm in length) depositing on them. The novel branch-like nanocomposite brings about the abundant porous structure as well as the large surface area (upto 42.8 m^2/g). In addition, their visible-light photodegradations toward organic dyes, including Congo red (CR), methylene blue (MB), eosin red (ER), methyl orange (MO) were investigated. The excellent photocatalytic performances are attributed to their large surface, improved visible light absorption and high separation efficiency of the photogenerated electron/hole. Furthermore, the degradation process was further studied by varying the amount of α-Fe$_2$O$_3$ deposition. α-Fe$_2$O$_3$/TiO$_2$-3 possesses the best performance to efficiently decolor CR solution even at a high concentration 50 mg/L (160 min 94 mg/g), ascribing to the high adsorption capacity derived from the large surface, strong electrostatic interaction and structure match between α-Fe$_2$O$_3$/TiO$_2$-3 and CR. These α-Fe$_2$O$_3$/TiO$_2$ heterostructures exhibit the great potential for decontamination of organic pollutants in waste water under visible light.

1. Introduction

With industrialization and rapid population growth, the environmental pollution has steadily raised awareness of a potential global crisis and is becoming overwhelming concerns all over the world. Thereinto, the growing water contamination is one of the worst environmental problems, and the advancement of pollution-free technologies has become an urgent task. Among available strategies, photocatalysis was regarded as one of the most effective and economical ways to purify the contaminated water. [1-5]

Thus, in recent years, many kinds of semiconductor metal oxides, such as Bi_2O_3, Fe_2O_3, ZnO, TiO_2 and so forth, have been developed as the catalyst to treat contaminations. [6-14] Among them, TiO_2 as a widely used wide band-gap (rutile ~3.0, anatase ~3.2 eV) semiconductor has been extensively studied owing to its abundance, nontoxicity, and stability. [15-20] However, the rapid combination of an electron–hole pair (e^-/h^+) goes against the photocatalytic performance. Besides, the wide band-gap of TiO_2 always requires ultraviolet (UV) light to excite the generation of electron–hole pair to make sure the photocatalysis. Nevertheless, UV light takes up only a small fraction (below 10%) of the sun's energy compared to visible light (about 44%).[21] To improve the utilization of sun light and enhance the photocatalytic performance of TiO_2 catalysts, the decrease of the recombination rate of the photogenerated electrons-holes and improvement of the visible light response of TiO_2 should be paid attention. Currently, the doping by metal or non-metal ions, or through its combination with narrow band gap nanocrystalline semiconductor such as PbS, AgI, InP, CdSe, Ag_2S and Bi_2S_3, were carried out, revealing the enhanced

3

photocatalysis activity.[7, 22-33] Furthermore, compared with pure TiO_2 materials, TiO_2-based binary metal oxides usually exhibit improved thermal and hydrothermal stability that is vital for the repeatable behavior.[34]

It is known that hematite (α-Fe_2O_3), one of the stable forms of iron oxide under ambient condition, has attracted considerable attention due to its high stability, low cost, non-toxicity, environmentally friendliness, narrow band gap (2.0–2.2 eV), natural abundance and very high positive valence band edge potential. And the combination of TiO_2 with Fe_2O_3 to form the heterostructure was considered as the effective way to decrease the recombination rate of photogenerated electrons-holes and improve the visible light response of the catalyst.[35] The core–shell $Fe_2O_3@TiO_2$ nanocomposites were synthesized via a heteroepitaxial growth route using the Fe_2O_3 spindle as a hard template to display improved photocatalytic degradation activity for Rhodamine B dye under visible light irradiation.[32]

Besides the component, the structure of these composites also plays a significant part in photocatalysis performance. One-dimensional (1D) nanofibers with high length-to-diameter ratio and ultra large special surface area that provides plenty of active sites have been regarded as the potential materials to be used in photocatalysis. Furthermore, these nanofibers always possess the various porous structure derived by the accumulation of many nanoparticals that is beneficial to the vectorial transfer of photo-induced charge carriers through the grain boundaries, leading to the high separation efficiency of electron–hole pairs as well as the superior catalytic properties. In this work, we report a simple two-step route to synthesize branched 1D

α-Fe$_2$O$_3$/TiO$_2$ heterostructures by a combination of the electrospinning and hydrothermal method. Congo red (CR), methylene blue (MB), methyl orange (MO)，and eosin red (ER) were adopted as the model dye pollutants, and the photodegradations under the visible light were investigated in detail. Furthermore, the degradation kinetics was further surveyed by varying the amount of α-Fe$_2$O$_3$ nanorods to reveal that the ratio of α-Fe$_2$O$_3$/TiO$_2$ coupled with the adsorption capacity to determine the final photocatalytic efficiency.

2. Experimental

2.1 Materials

Polyvinylpyrrolidone (PVP, Mw=1,300,000), Iron chloride hexahydrate (FeCl$_3$·6H$_2$O) was purchased from Aladdin (China). N, N-dimethylformamide (DMF) was bought from Tianjin Fengchuan Chemical Co. (China). Glacial cetic acid was purchased from Tianjin Fuyu Chemical Co. (China)**.** Tetrabutyl titanate (TBOT, Ti(OC$_4$H$_9$)$_4$), Sodium sulfate (Na$_2$SO$_4$) was purchased from Sinopharm Chemical Reagent Co.,Ltd (China). Congo red (CR), methylene blue (MB), eosin red (ER) and methyl orange (MO)，were obtained from Tianjin Guangfu Chemical Co. (China). All the reagents were of analytical grade and used without further purification.

2.2 Preparation of TiO$_2$ nanofibers

In the typical procedure, 0.85 mL of tetrabutyl titanate (TBOT, Ti(OC$_4$H$_9$)$_4$) was added to a mixed solution containing 1.5 mL of glacial cetic acid and 3.58 mL of N,N-Dimethylformamide (DMF) and stirred continuously 2h. Then, 0.6 g of poly(vinyl pyrrolidone) (PVP) powder (Mw= 1 300 000) was added to the above

solution. Then stirring at room temperature for 6 h, and the precursor solution of

$PVP/Ti(OC_4H_9)_4$ composites was obtained. Subsequently, the viscous precursor

solution was then loaded into a 5 ml syringe connected to 7-gauge stainless steel

needle. A variable high voltage power supply (Gamma FL 32174) was used to provide

a high voltage (15 kV) for the electrospinning. The positive electrode of the high

voltage power supply was connected to the needle tip and the grounded electrode was

connected to an aluminum foil. Finally, the prepared precursor fibers were calcined at

500 ^oC for 3 h under air at a rate of 1 ^oC /min to obtain the pure TiO_2 nanofibers.

2.3 Fabrication of branched α-Fe_2O_3/TiO_2 heterostructures

In a typical procedure, $FeCl_3 \cdot 6H_2O$ (0.04 M) and Na_2SO_4 (0.04 M) were dissolved in

the 20 mL of H_2O under ultrasonication 30 min to become uniform solution. The

resulting solution and the obtained TiO_2 nanofibers (16 mg) were transferred into a

Teflon-lined stainless autoclave, sealed and maintained at 120 ℃ for 12 h. After it

was cooled to room temperature, the precipitate was collected, rinsed using deionized

water and finally dried at 60 ° C for 12 h. The last products were annealed to 400 ° C

for 2h. With different amount of $FeCl_3 \cdot 6H_2O$ and Na_2SO_4 in growth solution, the

resultant composites named as α-Fe_2O_3/TiO_2-1 (0.01 M), α-Fe_2O_3/TiO_2-2 (0.03 M),

α-Fe_2O_3/TiO_2-3 (0.04 M), and α-Fe_2O_3/TiO_2-4 (0.05 M), respectively.

2.4. Photocatalytic test

The photocatalytic activity was measured by the degradation of eosin red (ER),

Congo red (CR), methylene blue (MB) and methyl orange (MO), respectively. In a

typical process, 0.05 g of α-Fe_2O_3/TiO_2 sample was suspended in 200 ml Congo red

aqueous solution (10 mg/L). The suspensions were magnetically stirred 1h in the dark

to ensure adsorption/desorption equilibrium, and the solution was then exposed to the

Xenon lamp (HSX-F/UV300), which was placed at about 10 cm from the reactor. A

400 nm cut-off filter was placed above the reactor to cut off UV light. At given

irradiation time intervals, the samples were collected regularly to measure the Congo

red degradation by UV-vis spectroscopy. The α-Fe_2O_3/TiO_2-3 structures were then

separated from the solution by centrifuging, washed with ethanol to fully remove the

residual organic species, then reused for the next run. Finally, the experiments of the

photocatalytic degradation of eosin red aqueous solution, methylene blue and methyl

orange aqueous solution were also conducted under the same conditions. After the

photocatalytic test of degrading 10mg/L CR, the α-Fe_2O_3/TiO_2-3 heterostructure was

then separated from the solution by centrifuging, washing clean exhaustive with

ethanol to fully remove the residual organic species and dried in oven at 60℃ the

whole night, then reused for the next run to test the recycle ability.

2.5. Hydroxyl radical test

In the analysis of hydroxyl radical, 50 mg sample and 20 mL 5 mg/L coumarin

aqueous solution were fixed in a quartz reactor. The irradiation condition is the same

to that of the above photodegradation testing. Finally, a certain amount of the solution

was transferred into a Pyrex glass cell for the fluorescence measurement of 7-

hydroxyl coumarin under the light excitation of 324 nm.

2.6. Characterization

The phase and composition of the as-obtained products were characterized by X-ray

diffraction (XRD, Rigaku Dmax-rB, Cu Kα radiation, 40 KV, 100 mA). X-ray

photoelectron spectroscopy (XPS) was characterized using a PHI 5000 ESCA X-ray

photoelectron spectrometer with a monochromated Al Kα X-ray source (1486.6 eV) to

investigate the chemical structure of the materials. The morphology and microstructure

of the samples were characterized by scanning electron microscopy (SEM,

Hitachi-4800) and transmission electron microscopy (TEM, JEOL 2010EX). A

specific surface area analyzer (NOVA2000E) was used to measure the N_2

adsorption/desorption. The Brunauer –Emmett–Teller (BET) formula was further used

to calculate the specific surface area. The efficiency of the photocatalytic degradation

was analyzed by monitoring dye decolorization at the maximum absorption

wavelength, using a UV-Vis spectrometer (Shimadzu UV-2550). UV–Vis absorption

spectra of these samples were recorded at a Cary 4000 spectrophotometer in the

wavelength range of 200–800 nm. Zeta potential was carried out on Zeta PALS zeta

potential analyzer.

3. **Results and discussion**

The general synthesis of α-Fe_2O_3/TiO_2 involves two individual steps: the preparation

of TiO_2 nanofibers via electrospinning technology and the deposition of α-Fe_2O_3 by

hydrothermal reaction (Scheme 1). And the corresponding structure and morphology

of the composite were characterized by SEM and TEM as shown in Fig. 1. It can be

clearly observed that the TiO_2 substrates reveal the uniform nanofiber morphology

with length up to several micrometers and a relatively uniform diameter of ~70 nm

(Fig. 1a). And the staggered nanofibers make up a 3D interconnected framework

which can not only facilitate the continuous transfer of electrons but also provide a large surface area, making it an ideal supporting material for the deposition of α-Fe_2O_3. From the TEM image as displayed in Fig. 1b, all TiO_2 fibers are composed of a large amount of nanoparticles about 10–20 nm in size and the accumulation of these nanoparticles also brings plenty of porous structure. After the facile hydrothermal treatment, α-Fe_2O_3 nanorods deposit on almost the external surface of TiO_2 nanofibers, and the novel heterostructures looks like the branches as visible in inset of Fig. 1c. The diameter of the individual hierarchical α-Fe_2O_3 /TiO_2 increases to about 300 nm, much longer than those of the pristine TiO_2 nanofibers (Fig. 1c, d). TEM observations were performed to further confirm the unique heterostructures of α-Fe_2O_3/TiO_2 hybrid. It can be clearly observed that the nanostructures are composed of a TiO_2 nanofiber (70 nm in diameter) and α- Fe_2O_3 nanorods (100~200 nm in length and ~30 nm in diameter) and the TiO_2 nanofibers are uniformly covered by the nanorods, forming a typical branched heterostructure (Fig. 1e and f), which is highly in agreement with the observations from SEM images (Fig. 1c and d). The high-magnification TEM image (Fig. 1g) demonstrates that the interplanar spacing of 0.24 and 0.25 nm agrees well with the spacing of the (103) lattice plane of anatase TiO_2 (A) and (101) lattice plane of rutile TiO_2 (R), respectively. The measured lattice spacing of 0.37 nm corresponds to the (012) plane of hematite Fe_2O_3. Fig. 1h further demonstrates the single crystal structure of Fe_2O_3 nanorods with the lattice spacing of $d_{110} = 0.25$ nm. In addition, there are some pores present in each Fe_2O_3 nanorod. The obtained hybrid nanocomposites consist of porous nanofiber structures with a homogeneous

distribution of α-Fe$_2$O$_3$ nanorods, which can not only shorten ion-transport distance,

but also accelerate the redox reactions for photocatalytic degradation organic dyes.

Subsequently, by adjusting the amount of Fe sources, α-Fe$_2$O$_3$/TiO$_2$-1, α

-Fe$_2$O$_3$/TiO$_2$-2 andα-Fe$_2$O$_3$/TiO$_2$-4 were prepared as exhibited in Fig. 2. From Fig. 2,

all samples also reveal the TiO$_2$ fibers networks combined withα-Fe$_2$O$_3$ nanorods.

Furthermore, with the increase of the amount of Fe sources, the surface of the

composites becomes rougher and rougher derived from moreα-Fe$_2$O$_3$ nanorods with

bigger size growing on. As shown in Fig. 2f, further increasing Fe sources, theseα

-Fe$_2$O$_3$ nanorods tend to pyramidal structure about 200 nm in length of α

-Fe$_2$O$_3$/TiO$_2$-4.

XRD measurements were carried out to characterize the phase and crystal

structures and the typical XRD patterns of the as-prepared materials are shown in Fig.

3. All the diffraction peaks can be indexed to anatase TiO$_2$ (JCPDS No. 73-1764),

rutile TiO$_2$ (JCPDS No. 73-1765) and hematite α-Fe$_2$O$_3$ (JCPDS No. 89−0597). No

other impurity diffraction peaks are discovered, which confirms the purity of the

product. Moreover, with the increase of Fe sources, the diffractions of hematite

increase as well due to the more α-Fe$_2$O$_3$ nanorods with bigger size growth. Thus, it is

confirmed that the successful synthesis of α- Fe$_2$O$_3$ /TiO$_2$ heterostructure.

The chemical composition of α-Fe$_2$O$_3$/TiO$_2$-3 was further investigated by the

XPS technique. Fig 4a shows the survey-scan XPS spectra of α-Fe$_2$O$_3$/TiO$_2$, and the

chemical binding energies of C 1s, O 1s, Fe 2p, and Ti 2p suggest the present O, Fe,

and Ti elements, while the carbon peak originated from the adventitious carbon

(below 0.9 wt % from TG). The high-resolution XPS spectrum of Ti 2p shows that the

binding energies of Ti $2p_{3/2}$ and Ti $2p_{1/2}$ (Fig. 4b) were located at 458.66 and 463.8 eV,

which matched well with the typical binding energy values of TiO_2. The binding

energy situated around 710.77 and 723.86 eV correspond to Fe 2p3/2 and Fe2p1/2 of

Fe_2O_3, with the satellite peak at 718.57 eV which corresponds to Fe^{3+} in α-Fe_2O_3 (Fig.

4c).[35-38] The O 1s spectrum can be deconvoluted into peaks located at 529.74 eV and

531.27 eV (Fig. 4d), which are mainly attributed to crystal oxygen in the lattice, i.e.,

oxygen atoms that are bound to iron (Fe-O) and titanium (Ti-O). XPS analysis further

demonstrates the successful preparation of α-Fe_2O_3/TiO_2 nanocomposite.

In addition, N_2 adsorption/desorption analysis was applied to determine the

porous structure of these α-Fe_2O_3 /TiO_2 composites and TiO_2 nanofibers. The

adsorption/desorption isotherm and the corresponding BJH pore diameter distribution

curves of above five samples are presented in Fig. 5. From Fig. 5a, with the increase

of the pressure, the adsorption amount increases obviously. All the isotherms can be

ascribed to the typical H3 hysteresis loops, implying the accumulative porous

structure of the samples. From Fig. 5b, all samples reveal wide pore size distribution

that is because it is difficult for accumulation pore to possess the uniform pore size.

The increase of Fe source, the macropore about 10-30 nm in size is present derived

from α- Fe_2O_3 nanorods deposition. With various porous structures, all samples show

the large average surface area about 20.4, 36.2, 42.8, 41.2, and 14.7 m^2/g for

α-Fe_2O_3/TiO_2-1, α-Fe_2O_3/TiO_2-2, α-Fe_2O_3/TiO_2-3, α-Fe_2O_3/TiO_2-4 and pure TiO_2

nanofibers, respectively (Table 1). α-Fe_2O_3/TiO_2s reveal the increased surface area

compared with pure TiO$_2$ nanofibers owing to the new surface derived from α-Fe$_2$O$_3$ nanorod deposition.

Fig. 6 shows the comparison of diffuse reflectance spectroscopy of single TiO$_2$, commercial Fe$_2$O$_3$ and α-Fe$_2$O$_3$/TiO$_2$ composites. The pure TiO$_2$ nanofibers present the typical absorption with an intense transition in the UV region, which could be assigned to the intrinsic band-gap absorption of TiO$_2$ (3.0, 3.2 eV). However, α-Fe$_2$O$_3$/TiO$_2$ should show enhanced absorption in the visible light region due to the visible sensitive component α-Fe$_2$O$_3$ (2.0–2.2 eV). The band gap energies estimated from the intercept of the tangents to the plots are 3.2 and 2.0 eV for the pure TiO$_2$ nanofibers and α-Fe$_2$O$_3$, agreeing well with the theoretical value. The band gap energy of the α-Fe$_2$O$_3$/TiO$_2$ nanocomposites can be confirmed by roughly comparing to the plot in Fig. 6b, which is obtained via the transformation based on the Kubelka–Munk function (F(R) =(1 - R)^2/(2R), where R = reflectance with the reflectance at 1000 nm set at 100%). And α-Fe$_2$O$_3$/TiO$_2$ complex reveal the decreased band gap energy (2.0-2.06 eV). With the more α- Fe$_2$O$_3$ deposition, the lower band gap energy can be found. The enhanced absorption in the visible light region of these α-Fe$_2$O$_3$/TiO$_2$ heterostructure is expected to induce the improved photocatalysis under visible light irradiation.

To demonstrate the photocatalytic activity of the as-synthesized samples toward organic dye pollutants, these α-Fe$_2$O$_3$/TiO$_2$ composites were adopted as the catalysts and the photocatalytic degradation tests toward CR were carried out. Fig. S1a-f present the absorption spectra of CR aqueous solution (initial concentration is 10

mg/L) in the presence of the samples under exposure to visible light for different durations. With the increase of the irradiation time, the absorption peak corresponding to CR at 498 nm diminishes gradually, testifying the degradation of CR. And the degradation rate curves are summarized in Fig. 7a. It takes 160, 160, 30, and 80 min for α-Fe_2O_3/TiO_2-1, α-Fe_2O_3/TiO_2-2, α-Fe_2O_3/TiO_2-3, and α-Fe_2O_3/TiO_2-4 to decolor about 77.2, 92.6, 95.1 and 94.1 % CR, respectively. In addition, the photocatalysis of TiO_2 nanofibers and commercial Fe_2O_3 towards CR also was investigated as contrast. As shown in Fig. S1e, under visible light irradiation for 160 min, merely 29.5 % of CR is decomposed by using the TiO_2 nanofibers as the photocatalyst. And pure Fe_2O_3 also reveals the degradation rate of 31.0 % toward CR at 160 min. From Fig. 7, α-Fe_2O_3/TiO_2 heterostructures reveal the improved visible light degradation capacity than the pure TiO_2 and Fe_2O_3. α-Fe_2O_3/TiO_2-3 exhibits the highest photocatalytic ability.

To further demonstrate the degradation process, the photocatalytic degradation kinetic was also investigated. The linear simulation of degradation of dye concentration can be accounted for by a pseudo first-order model, just so called the Langmuir-Hinshelwood (L-H) model. The L-H model is well established for heterogeneous photocatalysts (at low dye concentration). The relevant equation is as below:

$$r = -dC/dt = k'KC/1 + KC \qquad (1)$$

Where r is the rate of dye mineralization, k' is the rate constant, C is the dye concentration, and K is the adsorption coefficient. By integration, eqn (1) can be arranged into the following:

$$\ln(C/C_0)= -kt \qquad\qquad (2)$$

Where C_0 is the initial concentration of the dye solution and k is a rate constant. According to eqn (2), rate constant k can be given by the slope of fitting curves, when plotting $\ln(C/C_0)$ against. We are able to find out k from the gradient of the graph of $\ln(C/C_0)$ versus time (t) which is shown in Fig. 7b. All samples exhibit the good linear relationship between $\ln(C/C_0)$ and irradiation time t. From Fig. 7b, TiO_2 nanofibers displays lower rate constant $k = 0.00160$ min^{-1} that is because pure TiO_2 needs UV light to generate photogenerated electron-hole pairs to make sure the photodegradation. After the combination with α-Fe_2O_3, α-Fe_2O_3/TiO_2 heterostructures possess the enhanced degradative rate constant as well as the photocatalysis ability owing to the improved the utilization of visible light. α-Fe_2O_3/TiO_2-1 displays rate constant k=0.00637 min^{-1} more than TiO_2 nanofibers. As displayed in Fig. 6, with the increase of α-Fe_2O_3 the absorption of visible light is enhanced, so that α-Fe_2O_3/TiO_2-2 and α-Fe_2O_3/TiO_2-3 possesses the improved rate constant k = 0.01076 and 0.04336 min^{-1}. Further increasing of α-Fe_2O_3, the rate constant of α-Fe_2O_3/TiO_2-4 decreases to k=0.0158 min^{-1} that is caused by its decreased surface area/pore volume. The photocatalytic reactivity order is α-Fe_2O_3/TiO_2-3>α-Fe_2O_3/TiO_2-4>α-Fe_2O_3/TiO_2-2>α-Fe_2O_3/TiO_2-1> TiO_2 nanofibers >commercial Fe_2O_3. Based on the above investigation, the enhanced

14

visible light catalysis efficiency of α-Fe$_2$O$_3$/TiO$_2$ is ascribed to: 1) the improved visible light utilization owing to the doping of visible sensitive α-Fe$_2$O$_3$. 2) The spatial transfers of the visible-excited energetic electrons from α-Fe$_2$O$_3$ to TiO$_2$ in favorable to promote the separation and to prolong the lifetime of photogenerated charge carriers. [39] 3) The decreased charge transportation resistance of the heterojunction interface. 4) The high surface area and pore volume derived from the novel branch-like heterostructure that is benefit of the dyes toward the surface of the catalyst to enhance the degradation. The fastest degradation ability of α-Fe$_2$O$_3$/TiO$_2$-3 is derived from the largest surface area (42.8 cm^2/g) and appropriate content of the two components. [40]

Considering the excellent performance of α-Fe$_2$O$_3$/TiO$_2$-3 on dye decomposition, photocatalytic degradation activities of α-Fe$_2$O$_3$/TiO$_2$-3 heterostructure to ER, MB, and MO dyes were also investigated. Fig. S2a-c displays the UV/Vis absorption spectra of dyes in the presence of α-Fe$_2$O$_3$/TiO$_2$-3 heterostructure under visible light at different time intervals. From Fig. S2a-c, it is clearly seen that the absorption peaks corresponding to dyes diminish gradually with the illumination time prolonged, implying the degradation of dyes. And the photocatalytic activities of α-Fe$_2$O$_3$/TiO$_2$-3 toward the four dyes are summarized in Fig.8. As exhibited in Fig. 8, α-Fe$_2$O$_3$/TiO$_2$-3 reveals the fastest degradation toward CR, about 95.1 % decolored efficiency in 30 min. At the same time, just about 76.7 % ER and 15.3 % MB is degraded. And after 90 and 160 min irradiation, degradation percentage reaches 98.4 % and 67.6 % for ER and MB, respectively. However, it displayed the poor degradation evolution of MO

(1.1%, 160 min). It is known that, the high adsorption capacity benefits for the dye molecules close to the catalyst and always induces the enhanced the degradation rate. [41] From Fig.8, after the dark treatment, α-Fe$_2$O$_3$/TiO$_2$-3 reveals about 80.3, 35.0, 0.5 and 0.9 % adsorption amount for CR, ER MB and MO. Thus it is believed that the fastest degradation to CR can be ascribed to the highest adsorption capacity. Based on the previous reports, the adsorption capacity would be ascribed to the interaction and structure/size matching between the adsorbent and the adsorbate. It is known to all that, CR is a typical anionic dye that would possess the strong electrostatic interaction with α-Fe$_2$O$_3$/TiO$_2$-3 (Zeta potential: 2.50 ± 1.57 mV). Furthermore, the 1D fiber structures always reveal the high adsorption capacity to 1D long-chain dye, such as CR, so α-Fe$_2$O$_3$/TiO$_2$-3 exhibits the highest adsorption ability to CR. [42] However, the decreased adsorption capacity to the other anionic dye ER due to the low structure matching between the 2D planar molecular structure of ER and the 1D α-Fe$_2$O$_3$/TiO$_2$-3 nanofibers (with the slit pore). As shown in Fig.8, α-Fe$_2$O$_3$/TiO$_2$-3 displays the faster degradation rate of ER than that of MB and MO, the fast degradation rate of ER makes 98.4% degradation within 90 min irradiation.

To further investigate photo-degradation of α-Fe$_2$O$_3$/TiO$_2$-3 toward CR, various CR solutions (10-50 mg/L) were further used to demonstrate the adsorption and degradation activity of α-Fe$_2$O$_3$/TiO$_2$-3. As shown in Fig. S3a-d, it costs 30, 160, 160, 160 and 160 min for α-Fe$_2$O$_3$/TiO$_2$-3 to decompose about 95.1 % (10 mg/L), 81.5 % (20 mg/L), 63.7 % (30 mg/L), 54.9 % (40 mg/L) and 47.0 % (50 mg/L) CR, respectively. And the equilibrium adsorption isotherm (dark treatment) of

16

α-Fe_2O_3/TiO_2-3 to CR solution was calculated as exhibited in Fig. 9a. With the increase of the dye concentration, the adsorption amount increases dramatically until the adsorption reaches saturation (47.9 mg/g) that is a rather high adsorption amount. Furthermore, as revealed in Fig. 9a, the adsorption isotherm belongs to a type I curve, characteristic of a Langmuir isotherm. And the experimental equilibrium adsorption of dye on the sample was also analyzed by fitting the equilibrium adsorption data using the Langmuir equation:

$$\frac{c_e}{q_e} = \frac{1}{q_m k} + \frac{c_e}{q_m}$$

Where q_m is the theoretical maximum monolayer adsorption capacity (mg/g), k is the Langmuir constant, c_e is equilibrium concentration, and q_e is the equilibrium adsorption amount (mg/g). The corresponding linear Langmuir transform of the isotherm is exhibited in the Fig. 9a inset. From Fig. 9a inset, the adsorption behavior displays a good linear Langmuir relationship with the theoretical maximum adsorption values (q_m = 48.47 mg/g) close to the experimental capacity (47.9 mg/g). The good Langmuir adsorption relationship between CR and α-Fe_2O_3/TiO_2-3 associated with the high adsorption amount are expected to bring up the enhanced degradation capability. To visualize the degradation capability of α-Fe_2O_3/TiO_2-3 to CR, the variation of the degradation capability (dye/catalyst, mg/g) to degradation time was recorded as displayed in Fig. 9b. α-Fe_2O_3/TiO_2-3 displays 38.04 mg/g degradation capability for 10 mg/L CR under irradiation for 30 min. As increasing the CR concentration to 50 mg/L, the degradation capability increases to 94.0 mg/g after

160 min exposed in visible light. The high adsorption capacity benefits the dye molecules to be adsorbed on to the surface of the catalyst to enhance the photocalalysis performance. With the great decoloration capability, α-Fe$_2$O$_3$/TiO$_2$-3 is expected to possess the potential application on dye adsorption.

The 400 cut-off filter was used to make sure the irradiation wavelength is above 400 nm which can excite the electrons from the valence band (VB) of Fe$_2$O$_3$ to the different energy-level conduction band (CB), including the high-energy region (-0.16 eV to -1.0 eV/potential) and low energy region (0.1 eV to-0.16 eV/potential). In the high-energy region, some of the photogenerated electrons with the higher energy level than the CB position of TiO$_2$ (-0.16 eV/potential) could thermodynamically transfer to the CB of TiO$_2$ (Fig. 10), while photogenerated holes accumulated in the valence band of Fe$_2$O$_3$.[35, 43] The negative electrons in the valence band of TiO$_2$ will further react with molecular oxygen O$_2$ dissolved in the CR solution to form the superoxide anion O$_2^-$ and hydrogen peroxide H$_2$O$_2$. While the accumulated holes in the valence band of Fe$_2$O$_3$ will react with OH$^-$ species existing on the surface of the catalyst, producing reactive hydroxyl radicals (·OH).[32, 44-47]The reactions can be described as follows:

$$Fe^{3+} + h\gamma \rightarrow Fe^{2+} + Fe^{4+} + (h_{vb}^+ + e_{cb}^-)$$
$$Ti^{4+} + e_{cb}^- \rightarrow Ti^{3+}$$
$$e_{cb}^- (Ti^{3+}) + O_2 \rightarrow O_2^-$$
$$h_{vb}^+ (Fe^{4+}) + OH^- \rightarrow \cdot OH$$
$$OH \cdot + dyes \rightarrow degraded\ products$$
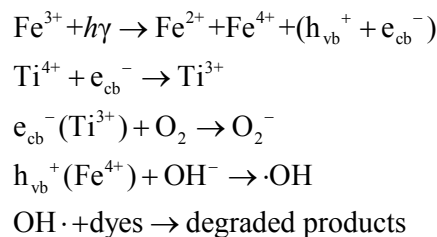
It is known that many dye molecules also can absorb a certain visible light, so that the contribution of the dye excitation to the photodegradation also should be considered. First, these dye molecules were excited from the ground state (Dye) to the

triplet excited state (Dye*) under the visible irradiation. This excited state dye species

is further converted into a semi-oxidized radial cation (Dye$^+$) by an electron injection

into the conduction band of TiO$_2$. Due to reaction between these trapped electrons and

dissolved oxygen in the system superoxide radical anions (O$_2$·$^-$) are formed which in

turn result into hydroxyl radicals (·OH) formation. These ·OH radicals are mainly

responsible for the oxidation of the organic compounds represented by the equations.

$$dye + h\gamma \rightarrow dye*$$
$$dye* + TiO_2 \rightarrow dye^+ + TiO_2^-$$
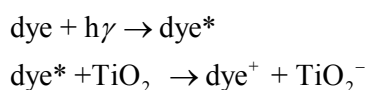
According to the previous investigation, the contribution of dye-sensitization to dye

degradation is much lower than the visible light initiated mechanism.[48-51]

And the radicals (•OH) measurement was carried out to study on charge

separation efficiency. Herein, the coumarin (C$_9$H$_6$O$_2$) fluorescent method is utilized to

detect the amount of •OH, in which the introduced coumarin could easily react with

•OH to produce luminescent 7-hydroxy-coumarin. Fig.11 α-Fe$_2$O$_3$/TiO$_2$-3 shows the

strongest fluorescent response at 449 nm, implying the most •OH generation. In

addition, these results are consistent with the photodegradation performance as

displayed in Fig. 7. Thus, in this paper it is believed that the high visible adsorption

and prolonged separation of the photogenerated electron/hole induce the excellent

performance on visible light degradation.[42]

The recyclable photocatalytic degradation results of CR in the presence of

α-Fe$_2$O$_3$/TiO$_2$-3 heterostructure for the 1st, 2nd, 3rd, 4th and 5th cycle are illustrated

in Fig.12. It is noted that even after 5 cycles, α-Fe$_2$O$_3$/TiO$_2$-3 heterostructure also

reveals 90 % purification for CR solution (10 mg/L), indicating that α-Fe$_2$O$_3$/TiO$_2$-3

heterostructure can be used as a recyclable catalyst for the degradation of CR under

visible light irradiation.

4. Conclusions

In summary，we report the synthesis of α-Fe$_2$O$_3$/TiO$_2$ with hierarchical branched

structure by a two-step process (electrospinning and hydrothermal approach). MB,

MO, CR, and ER were adopted as the model dyes and the photocatalytic tests were

carried out in detail. All α-Fe$_2$O$_3$/TiO$_2$ heterostructures reveal the enhanced visible

light degradation ability owing to the improved visible light adsorption and separation

of photogenerated electrons-holes. Especially, α-Fe$_2$O$_3$/TiO$_2$-3 possesses the most

efficient decoloration capacity (94.0 mg/g) to CR even at the high concentration (50

mg/L), attributing to the high surface area (42.8 m^2/g), appropriate proportion of the

two components, and the interaction/structural matching of catalyst and dye molecule.

The above factors should be paid great attentions on the design and synthesis of other

highly efficient visible-light photocatalysts. What more, the developed strategy would

provide us with a simple and feasible route to greatly improve the photocatalytic

performance of visible-response nano-semiconductors.

References

1. S. T. Kochuveedu, Y. H. Jang and D. H. Kim, *Chemical Society Reviews*, 2013, **42**, 8467-8493.

2. W. J. Ong, L. L. Tan, S.-P. Chai, S. T. Yong and A. R. Mohamed, *Nanoscale*, 2014, **6**, 1946-2008.

3. X. Xu, G. Yang, J. Liang, S. Ding, C. Tang, H. Yang, W. Yan, G. Yang and D. Yu, *Journal of Materials Chemistry A*, 2014, **2**, 116-122.

4. Q. Guo, C. Zhou, Z. Ma, Z. Ren, H. Fan and X. Yang, *Chemical Society Reviews*, 2015.

5. W. Zhou, G. Du, P. Hu, G. Li, D. Wang, H. Liu, J. Wang, R. I. Boughton, D. Liu and H. Jiang, *Journal of Materials Chemistry*, 2011, **21**, 7937-7945.

6. F. Qin, H. Zhao, G. Li, H. Yang, J. Li, R. Wang, Y. Liu, J. Hu, H. Sun and R. Chen, *Nanoscale*, 2014, **6**, 5402-5409.

7. W. Xitao, L. Rong and W. Kang, *Journal of Materials Chemistry A*, 2014, **2**, 8304-8313.

8. Z. Wu, H. Wang, Y. Xue, B. Li and B. Geng, *Journal of Materials Chemistry A*, 2014, **2**, 17502-17510.

9. Z. Zhao, J. Tian, D. Wang, X. Kang, Y. Sang, H. Liu, J. Wang, S. Chen, R. I. Boughton and H. Jiang, *Journal of Materials Chemistry*, 2012, **22**, 23395-23403.

10. X. Wang, L. Yin and G. Liu, *Chemical Communications*, 2014, **50**, 3460-3463.

11. Y. R. Smith, K. Joseph Antony Raj, V. Subramanian and B. Viswanathan, *Colloids*

and Surfaces A: Physicochemical and Engineering Aspects, 2010, **367**, 140-147.

12. S. Ma, J. Xue, Y. Zhou, Z. Zhang and X. Wu, *CrystEngComm*, 2014, **16**, 4478-4484.

13. A. Ajmal, I. Majeed, R. N. Malik, H. Idriss and M. A. Nadeem, *RSC Advances*, 2014, **4**, 37003-37026.

14. H. Xu, S. Ouyang, L. Liu, P. Reunchan, N. Umezawa and J. Ye, *Journal of Materials Chemistry A*, 2014, **2**, 12642-12661.

15. J. L. Gole, J. D. Stout, C. Burda, Y. Lou and X. Chen, *The Journal of Physical Chemistry B*, 2003, **108**, 1230-1240.

16. R. Ghosh Chaudhuri and S. Paria, *Dalton Transactions*, 2014, **43**, 5526-5534.

17. L. Lin, H. Wang, H. Luo and P. Xu, *Journal of Photochemistry and Photobiology A: Chemistry*, **307–308**, 88-98.

18. X. Zhang, Y. Liu, S.-T. Lee, S. Yang and Z. Kang, *Energy & Environmental Science*, 2014, **7**, 1409-1419.

19. Z. Zhang, C. Shao, X. Li, Y. Sun, M. Zhang, J. Mu, P. Zhang, Z. Guo and Y. Liu, *Nanoscale*, 2013, **5**, 606-618.

20. J. Mu, C. Shao, Z. Guo, M. Zhang, Z. Zhang, P. Zhang, B. Chen and Y. Liu, *Journal of Materials Chemistry*, 2012, **22**, 1786-1793.

21. V. Pore, T. Kivela, M. Ritala and M. Leskela, *Dalton Transactions*, 2008, 6467-6474.

22. S. V. Kershaw, A. S. Susha and A. L. Rogach, *Chemical Society Reviews*, 2013, **42**, 3033-3087.

23. H. Zhao, H. Liang, B. A. Gonfa, M. Chaker, T. Ozaki, P. Tijssen, F. Vidal and D. Ma, *Nanoscale*, 2014, **6**, 215-225.

24. X. Wang, J. Yang, S. Ma, D. Zhao, J. Dai and D. Zhang, *Catalysis Science & Technology*, 2015.

25. H. Cheng, W. Wang, B. Huang, Z. Wang, J. Zhan, X. Qin, X. Zhang and Y. Dai, *Journal of Materials Chemistry A*, 2013, **1**, 7131-7136.

26. F. Zan and J. Ren, *Journal of Materials Chemistry*, 2012, **22**, 1794-1799.

27. S. B. Rawal, A. K. Chakraborty, Y. J. Kim, H. J. Kim and W. I. Lee, *RSC Advances*, 2012, **2**, 622-630.

28. C. Xing, Y. Zhang, Z. Wu, D. Jiang and M. Chen, *Dalton Transactions*, 2014, **43**, 2772-2780.

29. J. Tang, W. Gong, T. Cai, T. Xie, C. Deng, Z. Peng and Q. Deng, *RSC Advances*, 2013, **3**, 2543-2547.

30. F. Jiang, Q. Tian, M. Tang, Z. Chen, J. Yang and J. Hu, *CrystEngComm*, 2011, **13**, 7189-7193.

31. S. Chaguetmi, F. Mammeri, S. Nowak, P. Decorse, H. Lecoq, M. Gaceur, J. Ben Naceur, S. Achour, R. Chtourou and S. Ammar, *RSC Advances*, 2013, **3**, 2572-2580.

32. Y. Xia and L. Yin, *Physical Chemistry Chemical Physics*, 2013, **15**, 18627-18634.

33. Z. Zhang, D. Jiang, C. Xing, L. Chen, M. Chen and M. He, *Dalton Transactions*, 2015, **44**, 11582-11591.

34. W. K. Jo and N. C. S. Selvam, *Dalton Transactions*, 2015, **44**, 16024-16035.

35. P. Luan, M. Xie, X. Fu, Y. Qu, X. Sun and L. Jing, *Physical Chemistry Chemical Physics*, 2015, **17**, 5043-5050.

36. M. A. Mahadik, S. S. Shinde, V. S. Mohite, S. S. Kumbhar, A. V. Moholkar, K. Y. Rajpure, V. Ganesan, J. Nayak, S. R. Barman and C. H. Bhosale, *Journal of Photochemistry and Photobiology B: Biology*, 2014, **133**, 90-98.

37. N. Sobti, A. Bensouici, F. Coloma, C. Untiedt and S. Achour, *J Nanopart Res*, 2014, **16**, 1-10.

38. M. Wang, M. Pyeon, Y. Gonullu, A. Kaouk, S. Shen, L. Guo and S. Mathur, *Nanoscale*, 2015, **7**, 10094-10100.

39. M. Xie, Q. Meng, P. Luan, Y. Feng and L. Jing, *RSC Advances*, 2014, **4**, 52053-52059.

40. S. Guo, S. Han, B. Chi, J. Pu and J. Li, *ACS Applied Materials & Interfaces*, 2014, **6**, 4743-4751.

41. K. Rajeshwar, M. E. Osugi, W. Chanmanee, C. R. Chenthamarakshan, M. V. B. Zanoni, P. Kajitvichyanukul and R. Krishnan-Ayer, *Journal of Photochemistry and Photobiology C: Photochemistry Reviews*, 2008, **9**, 171-192.

42. Y. Dong, H. Lin, Q. Jin, L. Li, D. Wang, D. Zhou and F. Qu, *Journal of Materials Chemistry A*, 2013, **1**, 7391-7398.

43. P. Luan, M. Xie, D. Liu, X. Fu and L. Jing, *Scientific Reports*, 2014, **4**, 6180.

44. T. Madrakian, A. Afkhami, R. Haryani and M. Ahmadi, *RSC Advances*, 2014, **4**, 44841-44847.

45. S. J. A. Moniz, S. A. Shevlin, X. An, Z. X. Guo and J. Tang, *Chemistry – A*

European Journal, 2014, **20**, 15571-15579.

46. K. E. deKrafft, C. Wang and W. Lin, *Advanced materials*, 2012, **24**, 2014-2018.

47. W. Wu, S. Zhang, X. Xiao, J. Zhou, F. Ren, L. Sun and C. Jiang, *ACS Applied Materials & Interfaces*, 2012, **4**, 3602-3609.

48. F. Chen, Y. Xie, J. Zhao and G. Lu, *Chemosphere*, 2001, **44**, 1159-1168.

49. C. Galindo, P. Jacques and A. Kalt, *Journal of Photochemistry and Photobiology A: Chemistry*, 2000, **130**, 35-47.

50. F. Zhang, J. Zhao, T. Shen, H. Hidaka, E. Pelizzetti and N. Serpone, *Applied Catalysis B: Environmental*, 1998, **15**, 147-156.

51. Y. Ma and J. Yao, *Journal of Photochemistry and Photobiology A: Chemistry*, 1998, **116**, 167-170.

Scheme 1
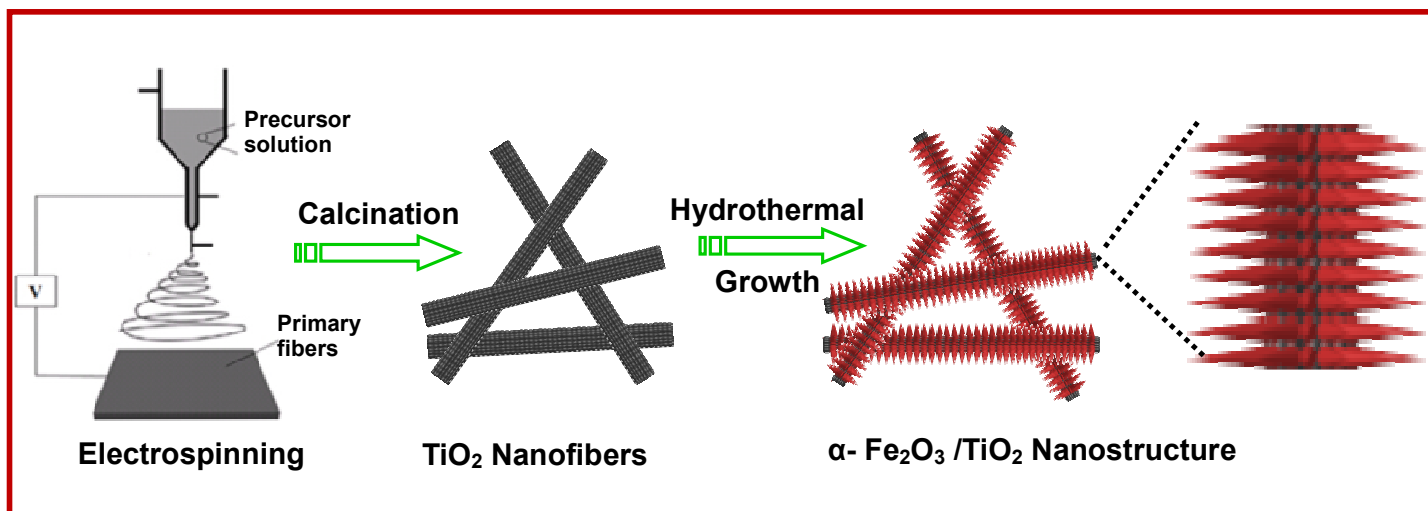
Fig. 1
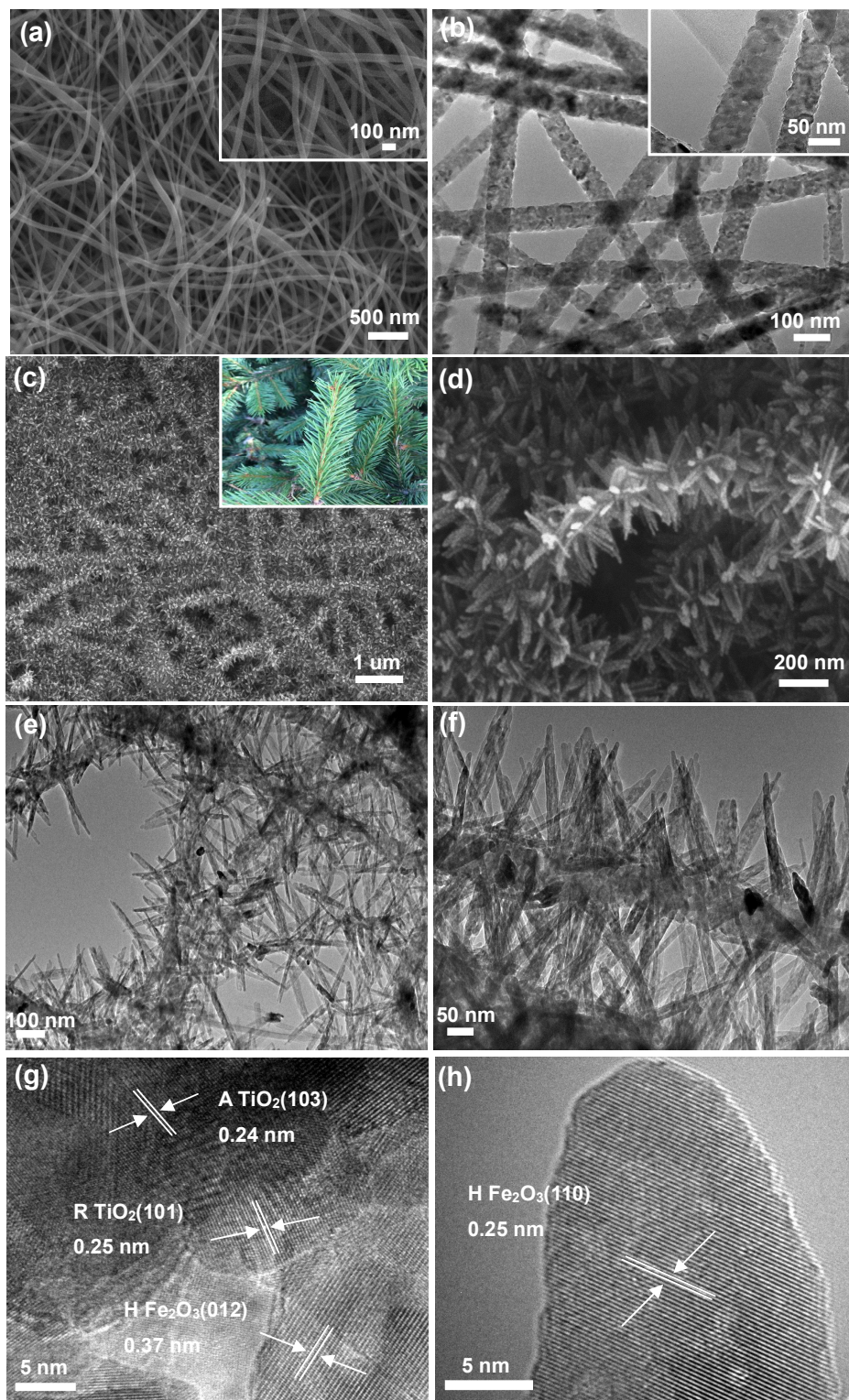
Fig. 2
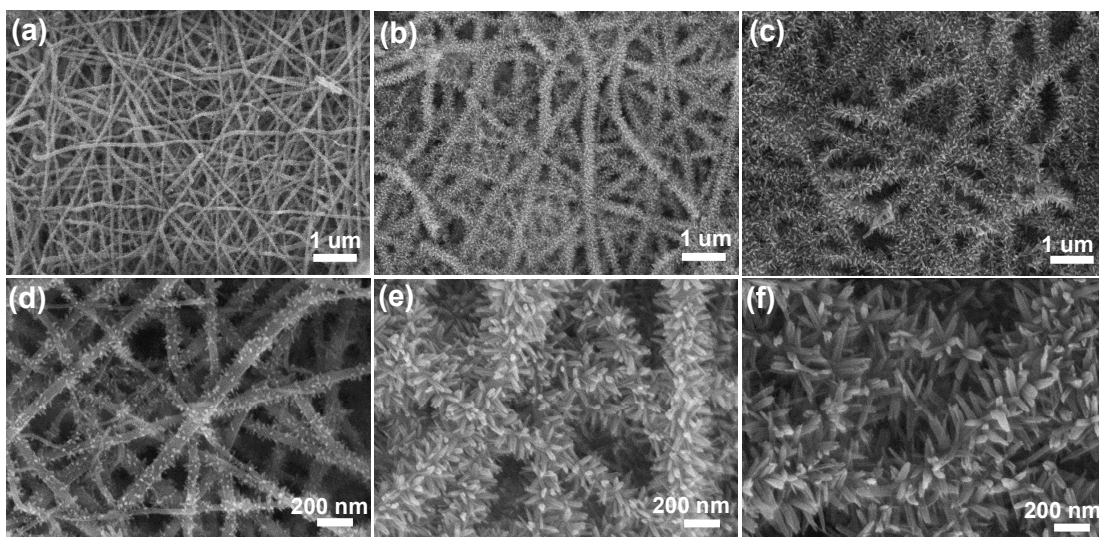
Fig. 3
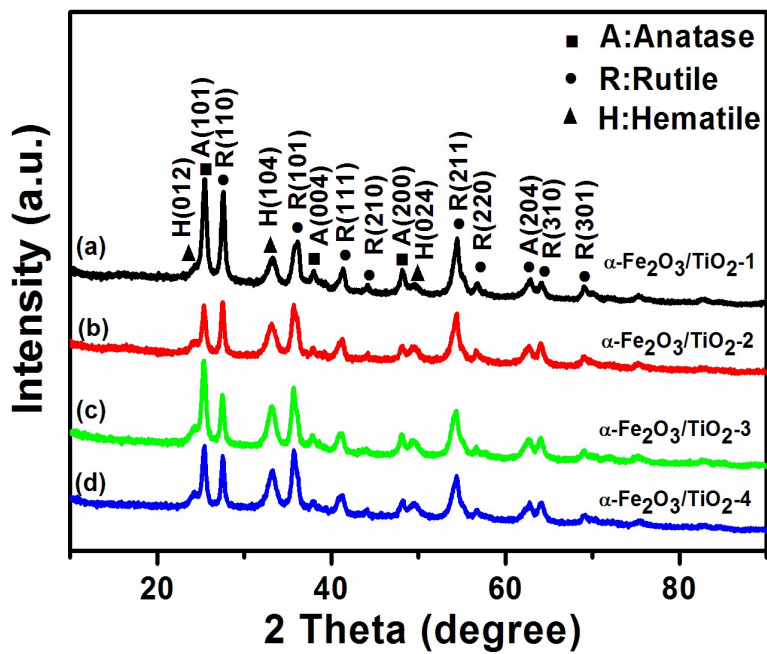
Fig. 4
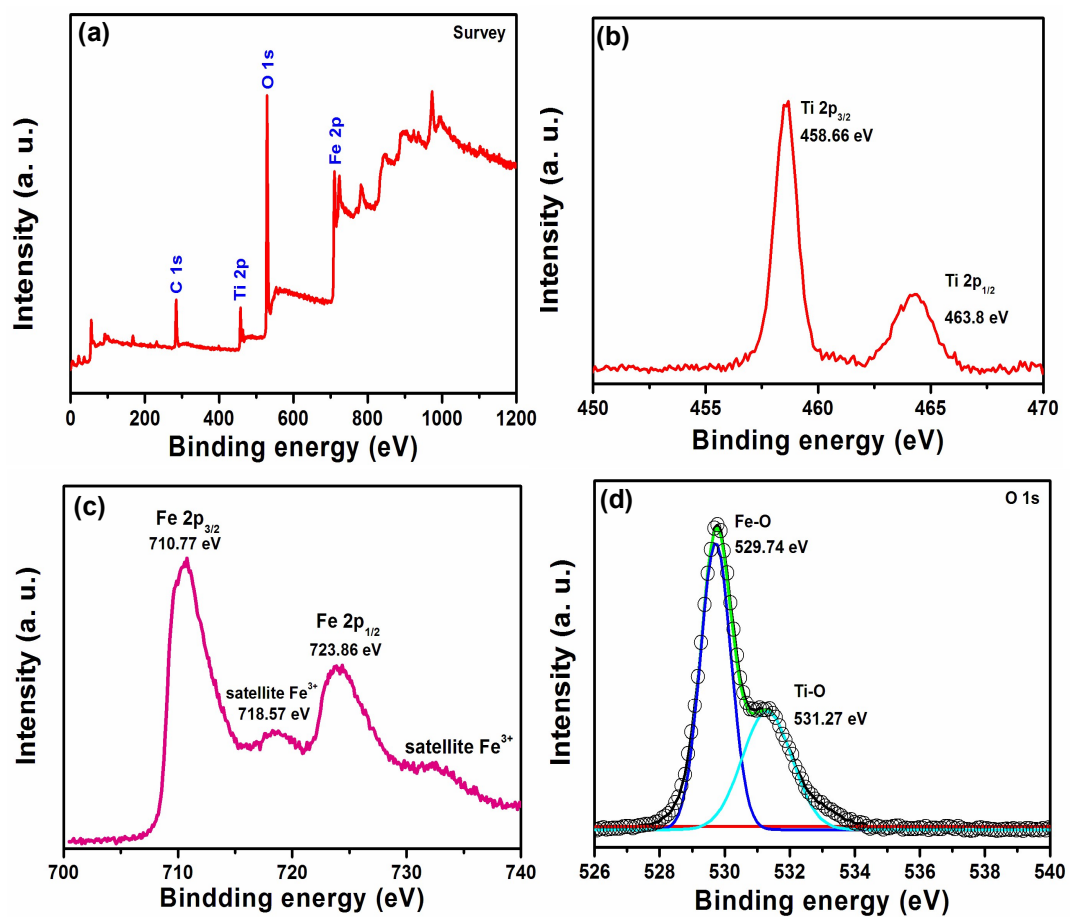
Fig. 5
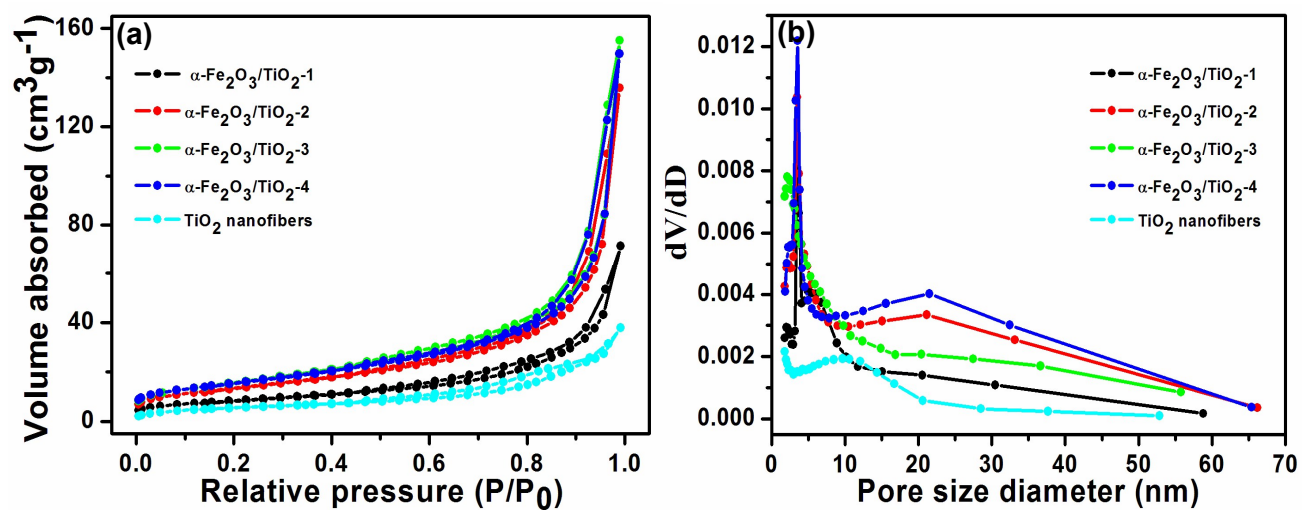
Fig. 6
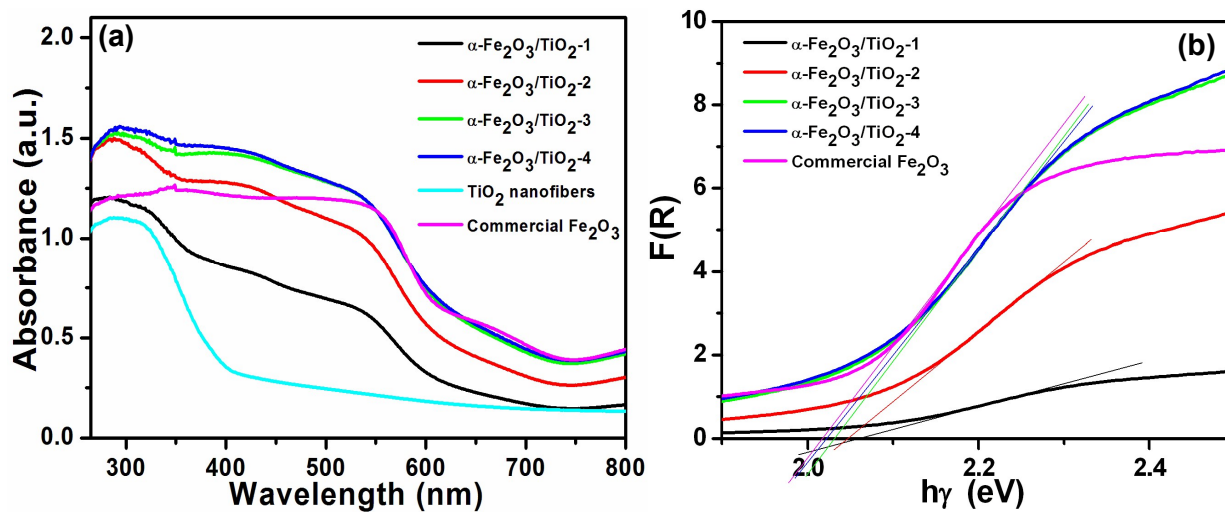
Fig. 7
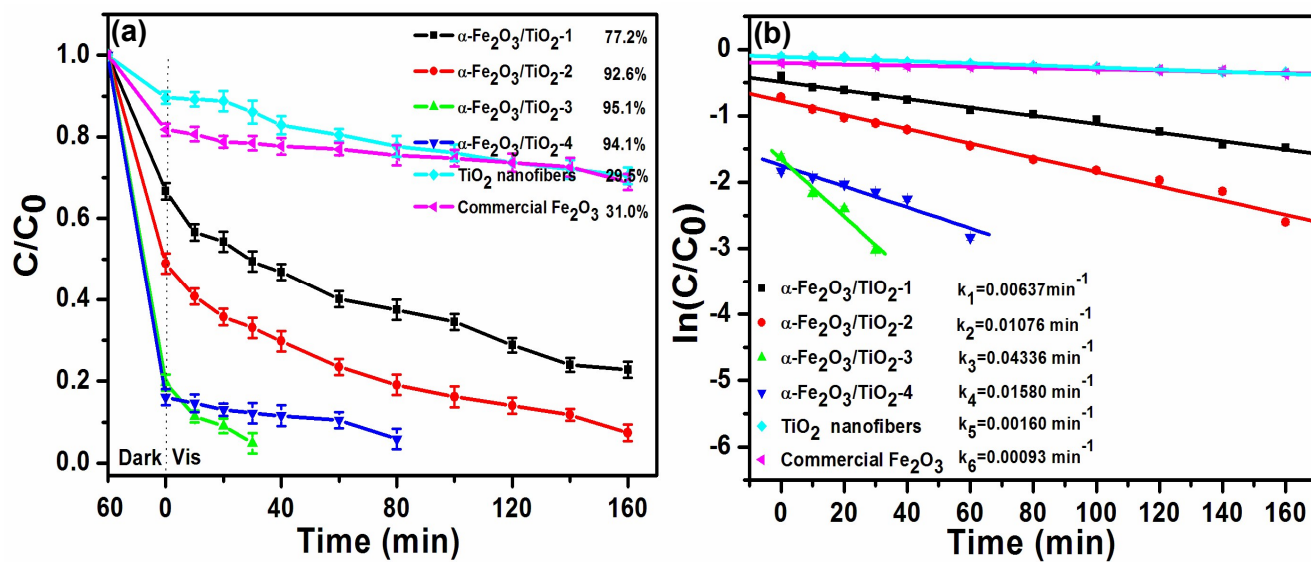
Fig. 8
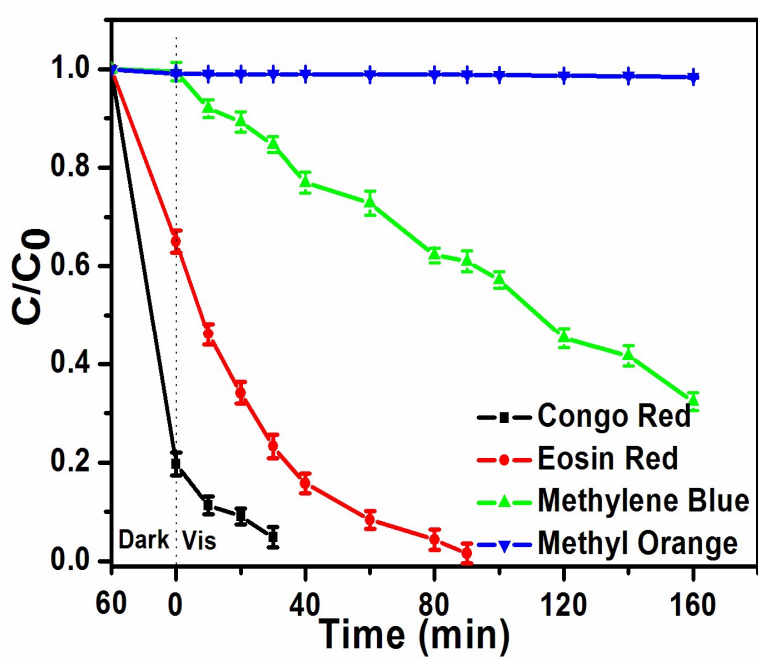
Fig. 9
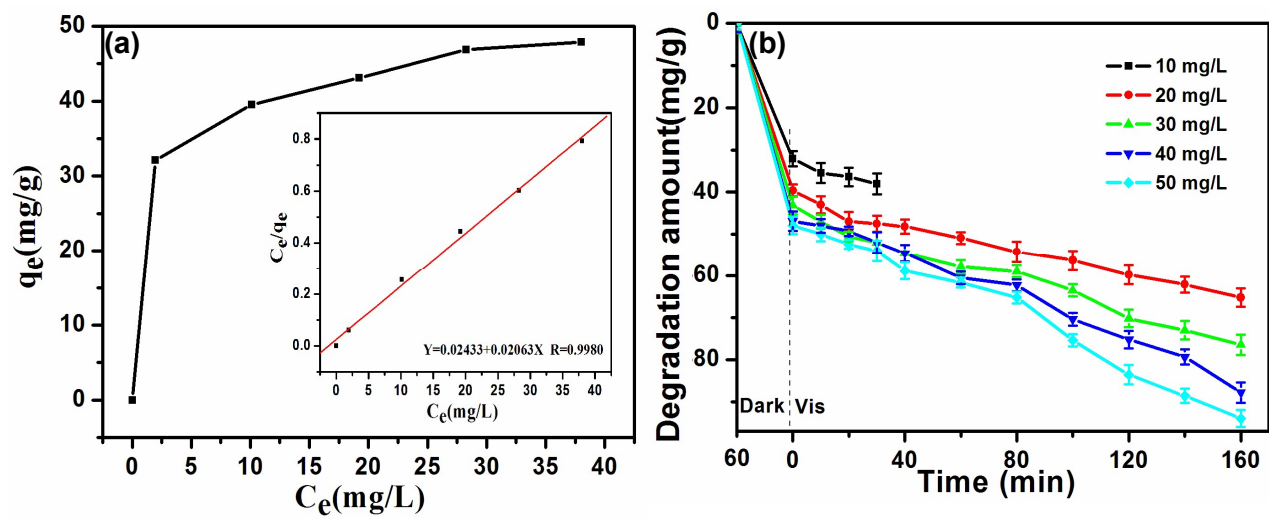
Fig. 10
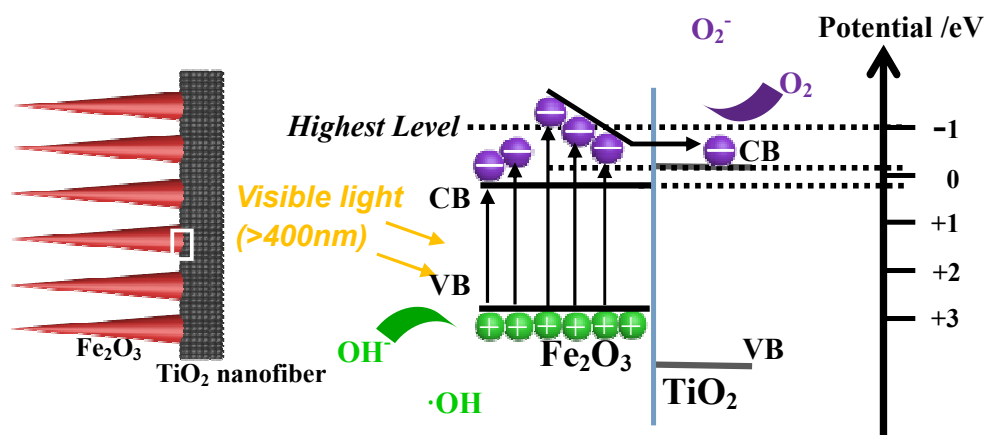
Fig. 11
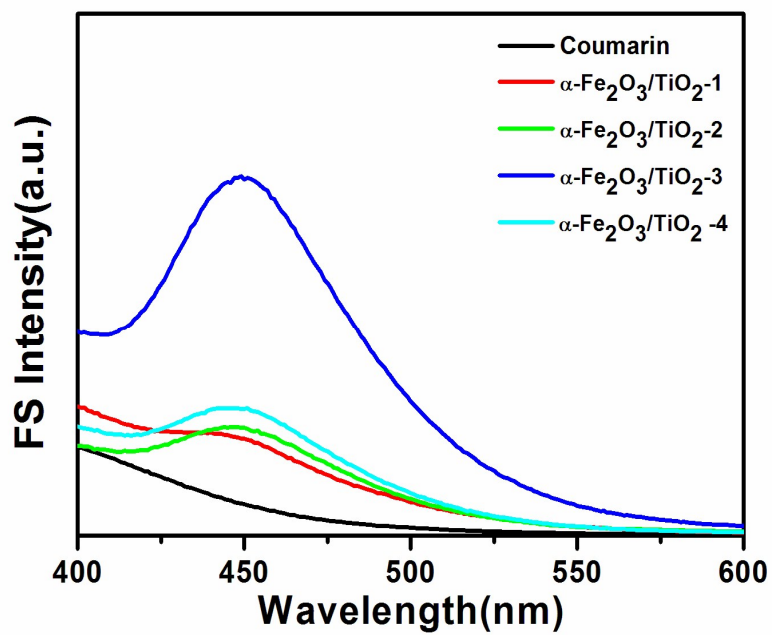
Fig. 12
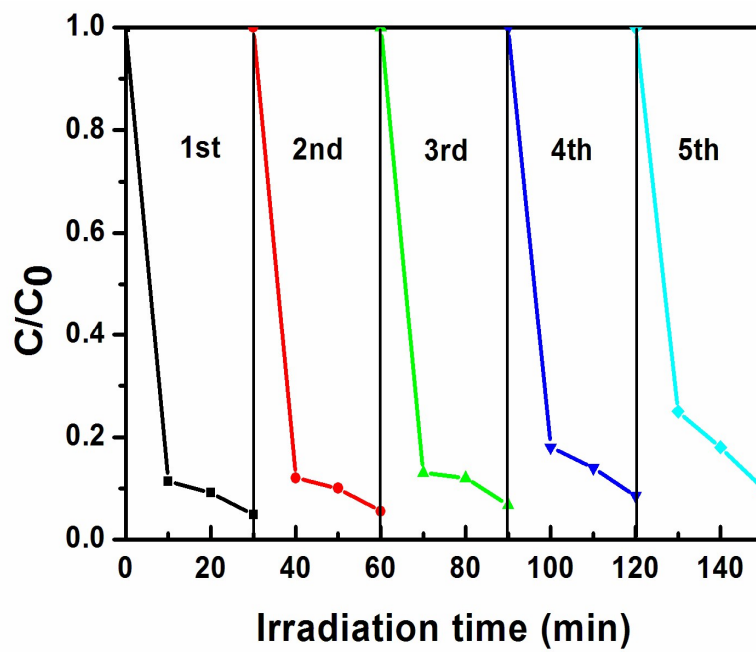
Table 1 The porous parameters of the samples.

Sample	Surface area[a] (m^2/g)	Pore volume[b] (cm^3/g)	Pore diameter (nm)
α- Fe_2O_3 /TiO_2-1	20.4±8.8	0.006±0.0007	3.44, 20.39
α- Fe_2O_3 /TiO_2-2	36.2±15.9	0.011±0.0012	3.44, 21.08
α- Fe_2O_3 /TiO_2-3	42.8±18.8	0.012±0.0017	2.12, 20.33
α- Fe_2O_3 /TiO_2-4	41.2±17.7	0.013±0.0021	3.48, 21.34
TiO_2 nanofibers	14.7±7.5	0.003±0.0007	1.71, 9.57

a,b: these data are calculated from three parallel assays.

Captions:

Scheme 1 The possible formation mechanism of α- Fe_2O_3/TiO_2 heterostructures.

Fig. 1 SEM images of the TiO_2 nanofibers (a) and α- Fe_2O_3/TiO_2-3 heterostructure (c, d). TEM images of TiO_2 nanofibers (b), TEM images (e, f) and the high-resolution TEM images (g, h) of α- Fe_2O_3/TiO_2-3.

Fig. 2 SEM images of α- Fe_2O_3/TiO_2-1 (a, d), α- Fe_2O_3/TiO_2-2 (b, e), and α-Fe_2O_3/TiO_2-4 (c, f).

Fig. 3 XRD patterns of the as-fabricated products: (a) α- Fe_2O_3/TiO_2-1, (b) α-Fe_2O_3/TiO_2-2, (c) α- Fe_2O_3/TiO_2-3 and (d) α- Fe_2O_3/TiO_2-4.

Fig. 4 Survey-scan XPS spectra α-Fe_2O_3/TiO_2 -3 (a); XPS Ti 2p spectra (b);XPS Fe 2p spectra (c); XPS O 1s spectra (d).

Fig. 5 N_2 adsorption-desorption isotherm (a) and BJH pore size distribution (b) of the five samples.

Fig. 6 (a) The UV–Vis absorption spectra of α- Fe_2O_3/TiO_2-1, α- Fe_2O_3/TiO_2-2, α-Fe_2O_3/TiO_2-3, α- Fe_2O_3/TiO_2-4, TiO_2 nanofibers and commerical Fe_2O_3, (b) The corresponding F(R) versus hγ curves.

Fig. 7 (a) Photocatalysis degradation rate of all samples, (b) Kinetic linear simulation curves of Congo red photocatalytic degradation under the visible light.

Fig. 8 Photocatalysis degradation rate of all the dyes of the α- Fe_2O_3/TiO_2-3 heterostructure irradiated by a visible light for different time periods.

Fig. 9 (a) Effect of the initial dye concentration, 10 mg/L, 20mg/L, 30mg /L, 40mg/ L and 50 mg/L, on the degradation capacity of the α- Fe_2O_3/TiO_2-3 heterostructure, and

the inset is the corresponding linear Langmuir transform of the isotherm; (b) variation

of the degradation capability of the α- Fe_2O_3/TiO_2-3 (dye/catalyst, mg/g) to

degradation time.

Fig. 10 The schematic of interfacial charge carries generation, transfer, and separation

between TiO_2 and Fe_2O_3 in the α- Fe_2O_3/TiO_2 heterostructure under the visible light.

Fig. 11 The fluorescence spectra for the formed hydroxyl radicals under visible

irradiation.

Fig. 12 Cycling tests of photocatalytic activity of the α- Fe_2O_3/TiO_2-3 heterostructure

for CR solution (10 mg/L) degradation.